Influence of the water content on the complex conductivity of bentonite

Jad El Alam, André Revil, Pierre Dick

Influence of the water content on the complex conductivity of bentonite

J. El Alam (1, 2), A. Revil (1), and P. Dick (2)

(1) Univ. Grenoble Alpes, Univ. Savoie Mont-Blanc, CNRS, UMR CNRS 5204, EDYTEM, 73370 Le Bourget du Lac, France

(2) Institut de Radioprotection et de Sûreté Nucléaire (IRSN), PSE-ENV/SEDRE/LETIS, 92260 Fontenay-aux-Roses, France

Corresponding Author: André Revil (andre.revil@univ-smb.fr),

Emails: pierre.dick@irsn.fr, jad.elalam@irsn.fr

Running title: Induced polarization of bentonite

Intended for publication in Engineering Geology

Abstract. Compacted bentonite is considered as a potential buffer material for deep geological disposals of high-level nuclear wastes. Methodologies to non-intrusively monitor the water content of such materials are important in the context of the safety of these storage facilities and for various engineering applications as well. Induced polarization is a non-intrusive geophysical method sensitive to the water content of porous media. We investigated the complex conductivity spectra of 69 samples made of 2 distinct MX80 bentonites, one in the form of powder from crushed pellets (Type I) and the other in the form of a granulated bentonite mixture (GBM, type II). The samples are prepared at different compaction states and saturations. The pore water conductivity of the core samples is estimated to be ~2.5 S m^{-1} (25°C) by two different methods. The complex conductivity spectra were obtained at room temperature (25±2°C) in the frequency range 1 Hz-45 kHz. In-phase and quadrature conductivities reflect conduction and polarization processes, respectively. At a given frequency, both the in-phase and quadrature conductivities increase with the water content along a trend that is independent of the compaction state. An induced polarization model based on the dynamic Stern layer model is used to explain these results. The first Archie's exponent is inferred from the formation factor using the in-phase conductivity data versus the pore water conductivity data at different salinities (NaCl, 25°C). The dynamic Stern layer model correctly predicts the dependence of the in-phase conductivity, quadrature conductivity, and normalized chargeability with the water conten and Cation Exchange Capacity (CEC). This petrophysical work can easily be applied to time-domain induced polarization data in field conditions.

Key words: Induced polarization; bentonite, water content; hydrogeophysics.

1. Introduction

Isolating high-level long-lived radioactive wastes from the biosphere is a priority across the world to avoid any significant release of radionuclides that may be dangerous to humankind (Madsen, 1998; Volckaert et al., 2004). In this context, Deep Geological Repositories (DGR) are foreseen to contain radioactive wastes in a tight and stable geological formation at depths of several hundred of meters. DGRs are designed to be passively safe and not reliant on active safety systems that would necessitate support from future generations. The post-closure passive safety principally relies on specifically designed engineered barriers (e.g., waste packages and engineered backfill materials) and host rock properties that will inhibit and reduce the migration of radioactive wastes (Madsen, 1998; Volckaert et al., 2004; Okko and Rautjaervi, 2006; Pettersson and Loennerberg, 2008; Köhler et al., 2015; Norris, 2017).

In the concept of DGRs of high-level radioactive waste (HLW), a multi-barrier system is usually adopted. It includes bentonite and retaining structures with concrete (e.g. mechanical plug or structure liner in tunnels and shafts). Bentonite-based Engineered Barrier Systems (EBS) are generally envisioned as a potential solution for the repository design because of their low permeability, large swelling capacity and high retention properties, as well as thermal stability among other wanted characteristics (Kanno and Wakamatsu, 1992; Chapman 2006; Chen et al., 2014).

One of the options for the repository design is to place the bentonite in the form of high-density compacted blocks in the vicinity of waste canisters to effectively seal preferential pathways for the migration of fluids (Mokni et al., 2016; Norris, 2017; Guo and Fall, 2021). The initially unsaturated bentonite is expected to sorb the surrounding fluids and compounds to retard their migration to the biosphere. Its high swelling capacity should impose sufficient swelling pressure to ensure a good sealing performance (generally a large swelling pressure results in low permeability). At the opposite, the concrete will undergo some chemical effects

from groundwater and will thus degrade over time, generating a high-pH alkaline solution that will migrate into the compacted bentonite and alter its hydro-mechanical behaviour and possibly jeopardize the safety of the repository.

Though the relationship between compaction (commonly described by the dry density of the compacted bentonite) and the swelling pressure has been widely studied (e.g., Gens and Alonso, 1992, Studds et al. (1998); Cui et al., 2002; Komine, 2004), recent experimental results show that the swelling pressure increases exponentially as the dry density of compacted bentonite increases (Villar and Lloret, 2008; Schanz and Al-Badran, 2014). It also decreases as the salinity of the pore water solution increases (Alawaji, 1999; Suzuki et al., 2005; Karnland et al., 2007; Herbert et al., 2008; Komine et al., 2009; Chen et al., 2015; Sun et al., 2015). However, for densely compacted bentonites with a high pore fluid salinity, the swelling pressure decreases less significantly as the salt concentration increases (Karnland et al., 2005; Castellanos et al., 2008; Siddiqua et al., 2011; Zhu et al., 2013). Hence, understanding and being able to monitor and predict the swelling characteristics of bentonite through time, with regards to changing porewater chemistry, is essential to guarantee the long-term safety of DGRs.

In this framework, monitoring the porewater evolution (content and chemistry), and linking it to the bentonite's petrophysical parameters (CEC, specific surface, saturation, porosity, density, etc.) through time and space appears essential to assess and predict the long-term performance of an EBS. However, in a DGR, the direct monitoring of the EBS with wired sensors will probably not be achieved in the buffer as wires can provide a preferential pathway for water and thus for radionuclide leakage (White et al. 2017). Geophysics, particularly geoelectrical methods, is potentially an ideal way to overcome this problem as: (i) it can be designed in a non-intrusive manner; (ii) it is sensitive to variations in water and clay content; (iii) it allows dynamic phenomena to be monitored over time; and (iv) it allows local anomalies

to be captured that isolated sensors cannot detect. Among the electrical methods available, spectral induced polarisation (SIP) appears to be the most suitable method, as it is not only sensitive to variations in water content but also to the mineralogical and chemical variability of the water and is therefore very convenient to monitor the EBS (Cosenza et al. 2007; Hermans et al. 2015; Merritt et al. 2016; López-Sánchez et al. 2017; Wang et al. 2017).

Induced polarization is a non-intrusive method currently playing a key role in the realms of hydrogeophysics (Kemna et al., 2012; Ntarlagiannis et al., 2019) and biogeophysics (Martin, 2012; Revil et al., 2012; Martin et al., 2015). It has a long history in geophysics for which it was primary used for a long time for ore detection (Seigel, 2007). Induced polarization properties are sensitive to the water content of porous rocks and sediments (Börner, 1992; Schön, 1996). It is a low-frequency active technique looking not only at imaging electrical conductivity but also in the ability of porous media to store reversibly electrical charges when submitted to an electrical current (Vinegar and Waxman, 1984). In the absence of metallic particles, the storage of these charges is done through the polarization of the electrical double layer coating the surface of the grains (Dukhin and Shilov, 1974; Dias, 2000; Revil, 2013a, b). The relevant property is called normalized chargeability in time-domain induced polarization or quadrature conductivity in frequency-domain induced polarization. Both are proportional to each other.

In frequency-domain induced polarization, complex conductivity spectra are obtained in a broad low frequency-range, typically 1 mHz to 100 kHz, by looking at the amplitude of the conductance and the phase lag between the current and the electrical field. Previous studies have been undertaken to better understand the induced polarization response of clayey materials including shaly sands and sandstones (e.g., Vinegar and Waxman, 1984; Revil et al., 2013b), soils (Revil et al., 2017), clay-sand mixtures (Breede et al., 2012), source shales and mudrocks (Revil et al., 2013a), and argillites and clay-rocks (Kruschwitz and Yaramanci, 2004;

123 Comparon, 2005; Ghorbani et al., 2009; Jougnot et al., 2010a, b; Okay et al., 2013, 2014; Tartrat
124 et al., 2019). In addition, induced polarization properties can be influenced by the presence of
125 metallic ions in the pore water (Vaudelet et al., 2011) and pyrite present in black shames and
126 some mudrocks (Tartrat et al., 2019).

127 To the best of our knowledge, bentonite powders subjected to changes in saturation and
128 compaction state have never been evaluated with induced polarization so far. In this study, we
129 investigate the complex conductivity spectra of 69 core samples at different water contents
130 corresponding to different saturation rates and compaction states. Our goals of this study are
131 (1) to establish a database for the complex conductivity spectra of bentonite at different
132 compaction states and volumetric water contents. Saturations range from 35% to 100%,
133 volumetric water contents range between 16 % to 71%. (2) Our second goal is to explain the
134 observed trends found between complex conductivity spectra and saturation and compaction
135 states using the dynamic Stern layer model of induced polarization developed (see Revil, 2012;
136 2013). (3) Our final goal is to assess the suitability of the SIP method to monitor the spatial and
137 temporal petrophysical heterogeneities of bentonite seals in geological disposals.

138

139 ## 2. Theory

140 Induced Polarization (or complex conductivity) is a geophysical technique that involves
141 measuring the low-frequency response (<100 kHz) of a medium under the influence of an
142 applied alternating electrical field (Olhoeft, 1981; Börner, 1992). Measurements can also be
143 performed in either time-domain or frequency-domain (Kemna et al., 2012). When a harmonic
144 electric field $\mathbf{E} = \mathbf{E}_0 \exp(+i\omega t)$ (t refers to time) is applied, the complex conductivity σ^* is
145 characterized by its amplitude $|\sigma|$ (in S m^{-1}) and phase lag φ (in rad), which are both measured
146 using an impedance meter. We can define a complex conductivity as,

147 $$\sigma^*(\omega) = |\sigma| e^{i\varphi} = \sigma'(\omega) + i\sigma''(\omega), \quad (1)$$

where $\omega = 2 \pi f$ denotes the pulsation frequency, f the frequency (Hertz), i is the pure imaginary number, and σ' and σ'' denote the real (in-phase) and imaginary (quadrature or out-of-phase) conductivity, respectively. Since the in-phase conductivity is the conductivity in absence of polarization (zero phase), it refers to the process of pure conduction (i.e., charge electromigration) while the quadrature conductivity refers to the mechanism of pure reversible charge storage, both under the action of an applied electrical field. Thus, such a decomposition is useful in terms of the underlying physics instead of dealing with amplitude and phase of the impedance.

In order to further understand induced polarization, we need to scale our analysis to the particle size. The polarization of a clay particle (smectite in the case of bentonite) is associated with the polarization of the electrical double layer coating the surface of the grains (Figure 1). This double layer comprises an inner layer called the Stern layer and an outer layer called the Gouy-Chapman layer.

The in-phase conductivity depends on two contributions corresponding to the bulk and surface conductivities. The bulk conductivity refers to conduction in the water phase located in the pore space while the surface conductivity is characterized by conduction in the electrical double layer coating the surface of the grains. At a given frequency, the in-phase conductivity can be expressed in the high salinity asymptotic limit by (see Revil et al., 2021, and references therein):

$$\sigma'(\omega) = \theta^m \sigma_w + \sigma_S(s_w, \omega), \quad (2)$$

where σ_w (S m^{-1}) denotes the pore solution conductivity, $\theta = s_w \phi$, θ denotes the dimensionless volumetric water content (s_w is the saturation and ϕ is the connected porosity, both dimensionless), and the exponent m (dimensionless) is called the first Archie exponent, the cementation exponent, or the porosity exponent. The formation factor F (dimensionless) is connected to porosity by $F = \phi^{-m}$ (Archie's law, Archie, 1942). Only in absence of surface

conduction in the electrical double layer coating the surface of the minerals and at saturation, the formation factor is given as the ratio of the resistivity of the porous material divided by the resistivity of the pore water. The quantity σ_s (S m^{-1}) denotes the surface conductivity associated with conduction in the electrical double layer. Since there is a lot of confusion in the literature regarding Archie's law, it is good to recall that Archie's law is not a conductivity equation and is valid whatever the strength of surface conductivity with respect to bulk conductivity associated with the pore water conductivity.

In order to interpret complex conductivity spectra in a partially-saturated and metal-free porous material, a model called the dynamic Stern layer model is required (e.g., Revil, 2013a, b, Revil et al., 2017). In the framework of this model, the complex conductivity is written as (Revil et al., 2017a)

$$\sigma^*(\omega) = \sigma_\infty - M_n \int_0^\infty \frac{h(\tau)}{1+(i\omega\tau)^{1/2}} d\tau \, , \tag{3}$$

where τ is a relaxation time (in s) and $h(\tau)$ denotes a (normalized) probability density for the relaxation times of the material. The real-valued quantity σ_∞ (S m^{-1}) corresponds to the instantaneous conductivity of the soil while the real-valued term σ_0 (S m^{-1}) corresponds to its DC (Direct Current) conductivity (Figure 1). Their expressions are further described below in terms of textural properties and environmental conditions. The normalized chargeability M_n corresponds to the difference between the instantaneous conductivity and the DC conductivity $M_n \equiv \sigma_\infty - \sigma_0$. Note that if the normalized chargeability is determined between two intermediate frequencies f_1 and f_2 (i.e., $M_n(f_1, f_2) = \sigma'(f_2) - \sigma'(f_1)$, $f_2 > f_1$), it is necessarily smaller than the integrated normalized chargeability $M_n \equiv \sigma_\infty - \sigma_0$ because the conductivity monotonically increases with the frequency.

The instantaneous and DC conductivities as well as the normalized chargeability of bentonite are given by

$$\sigma_\infty = \phi^m s_w{}^n \sigma_w + \phi^{m-1} s_w{}^{n-1} \rho_g B \mathrm{CEC}, \quad (4)$$

$$\sigma_0 = \phi^m s_w{}^n \sigma_w + \phi^{m-1} s_w{}^{n-1} \rho_g (B-\lambda) \mathrm{CEC}, \quad (5)$$

$$M_n = \phi^{m-1} s_w{}^{n-1} \rho_g \lambda \mathrm{CEC}, \quad (6)$$

where equation (6) results from equations (4) and (5), ρ_g denotes the grain density (2770 kg m^{-3} for smectite), and CEC denotes the cation exchange capacity of the soil expressed in C kg^{-1} or in meq/100 g (1 meq/100 g = 963.20 C kg^{-1} in SI units), B (in $m^2s^{-1}V^{-1}$) denotes the apparent mobility of the counterions for surface conduction (associated with the in-phase conductivity) and λ (in $m^2s^{-1}V^{-1}$) denotes the apparent mobility of the counterions for the polarization associated with the quadrature conductivity (see Vinegar and Waxman, 1984). We have $B(Na^+, 25°C) = 3.1\pm0.3\times10^{-9}$ $m^2s^{-1}V^{-1}$ and $\lambda(Na^+, 25°C) = 3.0\pm0.7\times10^{-10}$ $m^2s^{-1}V^{-1}$. A dimensionless number R was introduced by Revil et al. (2017) as $R = \lambda / B \approx 0.10\pm0.02$. The two mobilities are considered to be independent of the salinity.

When a clayey material is partially saturated with a pore water electrolyte and assuming that $m \approx n$, Revil (2013a, b) and Revil et al. (2021) obtained the following relationships from equations (4) to (6):

$$\sigma_\infty = \theta^m \sigma_w + \theta^p \rho_g B \mathrm{CEC}, \quad (7)$$

$$\sigma_0 = \theta^m \sigma_w + \theta^p \rho_g (B-\lambda) \mathrm{CEC}, \quad (8)$$

$$M_n = \theta^p \rho_g \lambda \mathrm{CEC}. \quad (9)$$

The case of the presence of metallic particles (like pyrite and magnetite) is discussed by Misra et al. (2016) but our bentonite core samples are free of such semi-conductors from X-Ray Diffraction (XRD) analysis.

Considering the quadrature conductivity at the geometric mean frequency of two frequencies f_1 and f_2 and the normalized chargeability defined as the difference between the in-phase conductivity at the frequency f_2(> f_1) and the in-phase conductivity at the lower

frequency f_1, we can connect the quadrature conductivity and the normalized chargeability with (Van Voorhis et al., 1973; Revil et al., 2017)

$$\sigma''\left(\sqrt{f_1 f_2}\right) \approx -\frac{M_n(f_1, f_2)}{\alpha}, \tag{10}$$

$$\alpha \approx \frac{2}{\pi}\ln A, \tag{11}$$

and A denotes the number of decades between f_1 and f_2 (for 3 decades, we have $A = 10^3$ and $\alpha \approx 4.4$). Equations (6) and (7) provide the relationship between the quadrature conductivity and the CEC. Equations (7) and (8) are not related to the dynamic Stern layer model and can be derived from the constant phase model. That said, as noticed in Revil et al. (2017a), they are very accurate for soils characterized by broad distribution of the relaxation times. From equation (7) and the expression of the surface conductivity, we can draw a relationship between the quadrature conductivity and the surface conductivity σ_S^∞ as

$$-\frac{\sigma''\left(\sqrt{f_1 f_2}\right)}{\sigma_S^\infty} = \frac{M_n(f_1, f_2)}{\alpha\sigma_S^\infty} = \frac{R}{\alpha}. \tag{12}$$

Since R and α are both constants (independent of frequency, temperature, and saturation), this means that the quadrature conductivity and the surface conductivity are proportional to each other. Equations (10) to (12) are exact for the constant phase model, which is characterized by the absence of peaks in the quadrature conductivity spectra. They are good approximation for the Cole Cole model (Revil et al., 2017c).

3. Materials and Methods

Our dataset of is made up of a total of 69 experiments (labelled from E1 to E69). Each experiment corresponds to a distinct core sample. Experiments E1 to E44 and E49 to E52 correspond to experiments made with crushed pellets sodium-MX80 bentonite and de-ionised water. The corresponding core samples are labelled MX80-Type I below. Experiments E45 to

247 E48 (MX80-Type I) are also made with the same crushed pellets sodium-MX80 bentonite
248 saturated with saline solutions of known conductivities. Experiments E53 to E69 are made
249 from a sodium-MX80 bentonite labelled GBM for highly compacted and granulated bentonite
250 mixture (Garitte et al., 2015). The corresponding core samples are labelled MX80-Type II
251 below.

252 Experiments E45 to E48 (between 90 – 100 % saturation) are used to calculate a
253 formation factor (then a cementation exponent) and surface conductivity using pore water
254 conductivities of 0.2, 1.0, 5.0, and 15 S m^{-1} (NaCl, 25°C) (Table 1). The conductivities of the
255 solutions used in making these samples were reached by mixing in NaCl with de-ionised water.
256 The data from Table 1 are shown in Figure 4 and fitted with the linear conductivity model,
257 which is valid above the so-called isoconductivity point (see Revil et al., 2017c).

258 The volumetric water content of each sample was determined using $\theta = m_w / (\rho_w V)$
259 where m_w denotes the total mass of water (in kg) in the sample (hygroscopic and added), ρ_w
260 is the mass density of water (in kg m^{-3}) and V (m^3) denotes the sample total volume (measured
261 using a caliper). The gravimetric water content is defined as $w = m_w / m_s$ where m_s denotes the
262 total mass of solid in the sample (in kg). The bulk and dry densities of the samples are then
263 given by $\rho_b = m / V$ and $\rho_d = \rho_b / (1 + w)$, respectively, where $m = m_w + m_s$ and V denotes the
264 total mass and total volume of the sample, respectively. The total volume of solids, voids and
265 water in the sample are respectively given by $V_s = m_s / \rho_g$, $V_p = V - V_s$, and $V_w = m_w / \rho_w$
266 where ρ_g is the grain density of bentonite (~2770 kg m^{-3}). We have also the following
267 definitions for the void ratio $e \equiv V_p / V_s$ (dimensionless), the connected porosity
268 $\phi = V_p / V = e / (1 + e)$ (dimensionless), and the water saturation $s_w = V_w / V_p$ (dimensionless).
269 The relationship between the volume water content θ and the gravimetric water content w is
270 therefore obtained after few algebraic manipulations as $\theta = w(\rho_g / \rho_w) / (1 - \phi)$.

To determine the pore water conductivity of our samples, we mixed 20 g of MX80 powder (crushed pellets) with 500 ml of deionised water, placed the mixture under an agitator for 48 hours and let it rest for 96 hours under room temperature and pressure. We then used a conductivity meter and measured a solution conductivity of 0.0594 S m^{-1} at 25°C. If we account for the dilution factor, the conductivity of the pore water is equal to 0.7 S m^{-1} at 25°C. Nevertheless, if we plot the conductivity of the sample E28 with respect to the saturated core samples saturated with NaCl solutions, we obtain a pore water conductivity of 2.5 S m^{-1}, much higher than anticipated. Considering the surface conductivity σ_S in equation (2) of 0.26 S m^{-1}, our experiments are clearly above the isoconductivity point (Figure 2) and therefore the linear relationships used in this paper are believed to be adequate (see Revil et al., 2017b).

Measurements of the cation exchange capacity (CEC) and specific surface area (SSA) of the bentonite have been performed by various authors in the literature (see Bradbury and Baeyens, 2002, Berger, 2008, Tang et al., 2008; and Karnland, 2010, for CEC, and Kiviranta and Kumpulainen, 2011, and Gomez and Villar, 2010, for SSA). We obtain the following values for the CEC and specific surface area of the MX-80 bentonite; 80 meq/100g, 31 m^2g^{-1} (BET method) and 573 m^2g^{-1} (EGME "Ethylene Glycol Monoethyl Ether" method) (see Bradbury and Baeyens, 2003; Bradbury et al., 2003; Molinero Guerra et al., 2017). In addition to this information, we performed new measurements of the CEC of the two bentonites (Type I and II) using cobaltihexamine method (see details in Guillaume 2002). We obtained a CEC of 81.9 ± 0.64 cmol(+)/kg (81.9 meq/100 g) for the crushed pellets MX80 (Type I) and 87.2 ± 0.64 cmol(+)/kg (87.2 meq/100 g) for GBM (Type II, 6 samples were used for replicates, 3 samples per bentonite).

The mineralogy of the bentonite is dominated by Montmorillonite (between 70 and 90% dry weight), with presence of Quartz, Feldspar, Muscovite and Calcite as well (Table 2). The hygroscopic water contents of both bentonites were determined, using oven drying at 105 °C

for a period of 120 hours, to be 6.07 (crushed pellets MX-80) and 8.64 for the GBM.

After mixing de-ionised water and bentonite powder in a mixing tray and using a spray, the mixtures are placed in a metallic sample holder that was manufactured especially for this purpose before being compressed using a uniaxial press (compression pressure depends on desired compaction state). The resulting cylindrical samples are 5 cm in diameter with a height generally comprised between 4 to 6 cm depending on the compaction state.

Complex conductivity spectra are obtained using a high-precision MFIA Impedance Analyzer manufactured by Zurich Instruments (Figure 2). Measurements were taken immediately after the creation of the samples to minimize the effect of drying (within minutes). A radial configuration of electrodes is used (Jougnot et al., 2009). All electrodes are placed at the centre height of the cylinder and at 90° from each other. Two current electrodes C1 and C2 impose the current and the potential electrodes P1 and P2 measure the potential at two points. The potential and current electrodes are disposable pre-gelled Ag-AgCl electrodes used in the medical industry (ECG). A geometrical factor is required to convert the impedance in terms of complex conductivity. It depends on electrode geometry and was numerically determined using COMSOL Multiphysics. We obtained values of 0.23 m and 0.25 m for sample heights of six and eight centimetres, respectively.

Depending on the sampling rate and frequency range chosen, conducting frequency sweeps on a sample takes a highly variable amount of time, ranging from 2-3 minutes for a range of 1 Hz to 45 kHz and at 100 sample points all the way to over 12 hours for 1 mHz to 45 kHz. Due to the number of samples analysed, we decide to explore a reduced frequency range comprised between 1 Hz and 45 kHz (Figure 3). We also conducted X-ray microtomography tests and found that our samples were mostly homogeneous (Figure 1).

4. Results

321 **4.1. Determination of the cementation exponent**

322 From samples E45 through sample E48, a linear relationship was determined between
323 the electrolyte (pore water) conductivity and in-phase conductivity of the core samples (Figure
324 4). The (intrinsic) formation factor F was determined to be 14 (determined at a porosity of
325 52%) and the surface conductivity $\sigma_S(s_w=1)=\phi^{m-1}\rho_g B\,\mathrm{CEC}$ was determined to be 0.26 S m^{-1}
326 by fitting a linear function $\sigma'=\sigma_W/F+\sigma_S$ to the (in-phase) conductivity data obtained at the
327 different salinities (Table 1 and Figure 4). Using Archie's law $F=\phi^{-m}$, the cementation
328 exponent is determined to be m=4.5.
329
330 **4.2. Prefactors**

331 Both in-phase and quadrature conductivities can be related to the volumetric water
332 content through power laws (Figures 5 and 6). The two power laws for the in-phase and
333 quadrature conductivity can be written as

334 $$\sigma'=\theta^m\sigma_w+\theta^p\Sigma_S, \tag{23}$$

335 $$\sigma''=\theta^p\frac{\Sigma_S R}{\alpha}, \tag{24}$$

336 $$M_n=\theta^p R\Sigma_S, \tag{25}$$
337

338 where $\Sigma_S\equiv\rho_g B\,\mathrm{CEC}$. Using ρ_g = 2800 kg m^{-3} (from crystallographic consideration regarding
339 the crystalline framework of smectite), B (Na$^+$, 25°C) =3.1×10^{-9} m^{2}s^{-1}V^{-1} and a CEC = 90
340 meq/100 g = 87×10^3 C kg^{-1} yields Σ_S = 0.75 S m^{-1}. With α = 8 and R = 0.10, the prefactor of
341 the power law relationship for the quadrature conductivity is a" = $\Sigma_S R/\alpha$ = 0.0095 S m^{-1}. If
342 the in-phase conductivity is dominated by the surface conductivity, the prefactor of the power-
343 laws relationship is a' = Σ_S = 0.75 S m^{-1}. These slopes agree with the results shown in Figures
344 5 and 6 for which a best fit yields a' = Σ_S = 1.1±0.1 S m^{-1} and a" = $\Sigma_S R/\alpha$ = 0.0100±0.0004

345 S m^{-1}.

346

347 ## 5. Discussion

348 Figure 7 shows a plot of the normalized chargeability versus the conductivity of the
349 core samples. When surface conductivity dominates the conductivity response, the data should
350 stick only the slope given by $R = 0.10$. We see that this is not the case for the core samples used
351 in the present study indicating in turn that the pore water conductivity may be larger than used
352 in our estimate above. In Figure 8, we check that the normalized chargeability taken between
353 two frequencies is proportional to the quadrature conductivity at the geometrical mean of the
354 two frequencies with a slope close to the predicted slope.

355 Bentonite is composed essentially of smectite, which has the largest CEC among clay
356 minerals. In Figure 9, we plot the surface conductivity versus the reduced CEC (CEC divided
357 by the tortuosity defined as the product of the formation factor by the connected porosity). The
358 data of bentonite core samples used for the salinity experiment is plotted among a large dataset
359 from the literature. Bentonite has clearly a very large surface conductivity above all other core
360 samples because of it very high cation exchange capacity. In Figure 10, we plot the normalized
361 chargeability versus the surface conductivity. Again, the magnitude of both the normalized
362 chargeability and surface conductivity of bentonite is above those of other rock samples. The
363 inclusion of other porous materials in Figures 9 and 10 indicates that the dynamic Stern layer
364 model applied to induced polarization is very general.

365 Another way to plot the in-phase and quadrature conductivity is through the dependence
366 with the bulk and dry densities of the material. Indeed, the difference between the bulk density
367 and the dry density depends linearly on the volumetric water content. In Figure 11, we plot the
368 in-phase and quadrature conductivity versus the difference between the bulk and dry densities
369 (see data in Table 3). As expected, we observed linear relationships in a log-log scale.

Another point we want to address in this section is the applicability of the proposed method to field conditions. The petrophysical investigations and results presented in this paper can be applied to time-domain induced polarization data obtained in field conditions. For instance, Abdulsamad et al. (2019) showed how induced polarization can be applied to estimate the change in water content in an embankment associated with a leakage. Similarly, time-domain induced polarization was recently applied to determine the transport properties of soil for agriculture (Revil et al., 2017c; Revil et al., 2021) and to landslides (Revil et al., 2020) using the dynamic Stern layer model of induced polarization described in the present manuscript. Indeed, if we know the pore water conductivity, equations (7) and (9) are two equations with two unknowns, the water content and the CEC. Tomography of time-domain induced polarization data can be perform to obtain tomograms of the conductivity and normalized chargeability. Then, we can apply these two equations to determine the water content and CEC tomograms. The conductivity of the pore water can be obtained using a speciation model accounting for the solubility of the minerals (see as an example for the Collavo-Oxfordian formation, Leroy et al., 2007).

6. Conclusion

In deep geological repository concepts, compacted bentonite is a material considered as a suitable barrier and an efficient buffer for radionuclides. We have performed complex conductivity spectra of 69 core samples at different water content with different porosities (compaction state) and saturation. The experiments have been mostly done at a low pore water conductivity of 0.059 S m^{-1} at 25°C. The following conclusions have been reached:

(1) Both the in-phase conductivity and quadrature conductivity exhibit a power law dependence with the (volumetric) water content.

(2) The prefactor coefficients for these power laws can be determined from the theory,

especially from the CEC of the bentonite alone.

(3) The values of the two power-law exponents $m = 4.5$ and $p = 3.1 \pm 0.1$ are consistent with the expression $p = m - 1$.

Further works are needed to extend the present database to a broader salinity range. Larger scale experiments in terms of time-lapse tomography of a large bentonite plug undergoing desaturation would be welcome to see how time-lapse induced polarization tomography can be used to assess the evolution of the water content in a bentonite-made structure. Induced polarization appears a promising method to assess the monitor the petrophysical characteristics of bentonites.

Acknowledgements: This work is funded by IRSN. We thank the two referees and the Editor for fruitful comments that have helped us to shape a better version of our paper.

References

Abdulsamad F., A. Revil, A. Soueid Ahmed, A. Coperey, M. Karaoulis, S. Nicaise, and L. Peyras, 2019, Induced polarization tomography applied to the detection and the monitoring of leaks in embankments dams and dikes. Engineering Geology, **254**, 89–101. https://doi.org/10.1016/j.enggeo.2019.04.001

Alawaji, H.A., 1999, Swelling and compressibility characteristics of sand–bentonite mixtures inundated with liquids. Appl. Clay Sci., **15** (3–4), 411-430.

Archie, G. E., 1942, The electrical resistivity log as an aid in determining some reservoir characteristics. SPE-942054-G, **146**, 54–62. https://doi.org/10.2118/942054-G.

Berger, J., 2008, Hydration of swelling clay and bacteria interaction: An experimental in situ reaction study, PhD Thesis, University Strasbourg 1.

Börner, F., 1992, Complex conductivity measurements of reservoir properties. Advances in Core Evaluation III (Reservoir Management): Gordon and Breach Science Publishers.

Bradbury, M. H, and B. Baeyens. 2003, Porewater Chemistry in Compacted Re-Saturated MX-80 Bentonite, Journal of Contaminant Hydrology, 8th International Conference on Chemistry and Migration Behaviour of Actinides and Fission Products in the Geosphere - Migration 01, **61** (1): 329–38. https://doi.org/10.1016/S0169-7722(02)00125-0.

Bradbury, M.H., Baeyens, B., 2002, Pore water chemistry in compacted re-saturated MX-80 bentonite: Physico-chemical characterisation and geochemical modelling (ISSN 1015–2636). Switzerland.

Breede, K., Kemna, A., Esser, O., Zimmermann, E., Vereecken, H., Huisman, J. A., 2012, Spectral induced polarization measurements on variably saturated sand-clay mixtures. Near Surface Geophysics, **10** , 479–489. https://doi.org/10.3997/1873-0604.2012048.

Castellanos, E., Villar, M.V., Romero, E., Lloret, A., Gens, A. 2008. Chemical impact on the hydro-mechanical behaviour of high-density FEBEX bentonite. Phys. Chem. Earth, **33**,

S516-S526

Chapman, N. A., 2006, Geological disposal of radioactive wastes-Concept, status and trends. J. Iberian Geology, **32** (1), 7–14.

Chen, Y.-G., Cui, Y.-J., Tang, A. M., Wang, Q., Ye, W.-M., 2014, A Preliminary study on hydraulic resistance of bentonite/host-rock seal interface. Géotechnique **64** (12), 997–1002. https://doi.org/10.1680/geot.13.p.209.

Chen, Y.G., Zhu, C.M., Ye, W.M., Cui, Y.J., Wang, Q., 2015, Swelling pressure and hydraulic conductivity of compacted GMZ01 bentonite under salinization–desalinization cycle conditions. Applied Clay Science, **114**, 454-460.

Comparon, L., 2005, Etude expérimentale des proprietes electriques et dielectriques des materiaux argileux consolides (PHD thesis). Institut de Physique du Globe de Paris – IPGP, 400 pp.

Cui, Y.J., Yahia-Aissa, M., Delage, P. 2002, A model for the volume change behavior of heavily compacted swelling clays. Engineering Geology, **64**, 233-250.

Dias C.A., 2000, Developments in a model to describe low-frequency electrical polarization of rocks. Geophysics, **65**, 437–451. https://doi.org/10.1190/1.1444738.

Dukhin S.S., Shilov V.N., 1974, Dielectrical phenomena and the double layer in disperse systems and polyelectrolytes. Wiley, New York.

Garitte B., Weber, H.P., Müller, H.R., 2015, LUCOEX Deliverable D2.3 – Requirements, manufacturing and QC of the buffer components. WP2 – Full-Scale Emplacement Experiment (FE) at Mont Terri. EU report downloadable from www.lucoex.eu.

Gens, A., Alonso, E., 1992. A framework for the behaviour of unsaturated clay. Can. Geotech. J., **29**, 1013-1032.

Guillaume, D., 2002, Etude expérimentale du système fer-smectite en présence de solution à 80 °C et 300° C. 207 pp., Doctoral dissertation, PhD. Thesis, Université de Nancy, France.

458 Ghorbani, A., Cosenza, P., Revil, A., Zamora, M., Schmutz, M., Florsch, N., and Jougnot, D.,
459 2009, Non-invasive monitoring of water content and textural changes in clay-rocks using
460 spectral induced polarization: A laboratory investigation. Applied Clay Science, **43**, 493–
461 502. https://doi.org/10.1016/j.clay.2008.
462 Gómez-Espina, R., and Villar, M.V., 2010, Geochemical and mineralogical changes in
463 compacted MX-80 bentonite submitted to heat and water gradients: Applied Clay Science,
464 **47**, 400–408. https://doi.org/10.1016/j.clay.2009.12.004.
465 Guo, G., Fall, M., 2021, Advances in modelling of hydro-mechanical processes in gas
466 migration within saturated bentonite: A state-of-art review: Eng. Geol., **287**, 106123.
467 https://doi.org/10.1016/j.enggeo.2021.106123.
468 Herbert, H.J., Kasbohm, J., Sprenger, H., Fernandez, A.M., Reichelt, C., 2008, Swelling
469 pressures of MX-80 bentonite in solutions of different ionic strength. Phys. Chem. Earth,
470 **33**, S327-S342.
471 Hernandez, G.M., 2002, Etude expérimentale de la sorption d'eau et du gonflement des argiles
472 par microscopie électronique à balayage environnementale (ESEM) et analyse digitale
473 d'images. PhD Thesis, Université Louis Pasteur - Strasbourg I. https://tel.archives-
474 ouvertes.fr/tel-00123521.
475 Jougnot D., Ghorbani A., Revil A., Leroy P., Cosenza P., 2010a, Spectral Induced Polarization
476 of partially saturated clay-rocks: A mechanistic approach: Geophysical Journal
477 International, **180**, 1, 210-224. https://doi.org/10.1111/j.1365-246X.2009.04426.x.
478 Jougnot, D., A. Revil, N. Lu, A. Wayllace, 2010b, Transport properties of the Callovo-
479 Oxfordian clay rock under partially saturated conditions. Water Resources Research, **46**,
480 8. https://doi.org/10.1029/2009WR008552.
481 Kanno, T., Wakamatsu, H., 1992, Water Uptake and Swelling Properties of Unsaturated
482 Bentonite Buffer Materials. Can. Geotech. J., **29**, 1102–1107. https://doi.org/10.1139/t92-

127.

Karnland, O., S. Olsson, U. Nilsson. 2006, Mineralogy and sealing properties of various bentonites and smectite-rich clay materials. ISSN 1404–0344. 43003619, Sweden.

Karnland, O., 2010, Chemical and mineralogical characterization of the bentonite buffer for the acceptance control procedure in a KBS-3 repository.

Karnland, O., Muurinen, A., Karlsson, F., 2005, Bentonite swelling pressure in NaCl solutions –Experimentally determined data and model calculations. E.E. Alonso, A. Ledesma (Eds.), Advances in Understanding Engineered Clay Barriers: Proceedings of the International Symposium on Large Scale Field Tests in Granite, Sitges, Barcelona, 12–14 November 2003, Taylor and Francis Group, London, 241-256.

Karnland, O., Olsson, S., Nilsson, U., Sellin, P., 2007. Experimentally determined swelling pressures and geochemical interactions of compacted Wyoming bentonite with highly alkaline solutions. Phys. Chem. Earth, 32 (1) (2007), pp. 275-286

Kemna A., Binley A., Cassiani G., Niederleithinger E., Revil A., Slater L., Williams K.H., Flores O.A., Haegel F.-H., Hördt A., Kruschwitz S., Leroux V., Titov K., Zimmermann E., 2012, An overview of the spectral induced polarization method for near-surface applications. Near Surf Geophysics, **10**, 453–468. https://doi.org/10.3997/1873-0604.2012027.

Kiviranta, L., Kumpulainen, S., 2011, Quality Control and Characterization of Bentonite Materials.

Köhler, S., T., F., Müller, H., Gaus, I., 2015, Swiss backfilling concept – Requirements and approaches for optimization of the bentonite barrier around SF/HLW disposal canisters.

Komine, N. Ogata, 1994, Experimental study on swelling characteristics of compacted bentonite. Can. Geotech. J., **31**, 478-490.

507 Komine N., Komine H., Yasuhara K., Murakami S.., 2009, Swelling characteristics of
508 bentonites in artificial seawater. Can. Geotech. J., **46**, 2, 177-189.
509 Kruschwitz S., Yaramanci, U., 2004, Detection and characterization of the disturbed rock zone
510 inclaystone with the complex resistivity method. Journal of Applied Geophysics, **57**, 63–
511 79. https://doi.org/10.1016/j.jappgeo.2004.09.003.
512 Kumpulainen, S., and L. Kiviranta. 2010. Mineralogical and Chemical Characterization of
513 various bentonite and Smectite-Rich Clay Materials Part A: Comparison and Development
514 of Mineralogical Characterization Methods Part B: Mineralogical and Chemical
515 Characterization of Clay Materials." Finland, 43066642.
516 Leroy, P., Revil, A., 2009. A mechanistic model for the spectral induced polarization of clay
517 materials. Journal of Geophysical Research : Solid Earth **114**, B10202.
518 https://doi.org/10.1029/2008JB006114.
519 Leroy, P., Revil, A., 2004. A triple-layer model of the surface electrochemical properties of clay
520 minerals. Journal of Colloid and Interface Science, **270**, 371–380.
521 https://doi.org/10.1016/j.jcis.2003.08.007.
522 Leroy, P., A. Revil, S. Altmann, and C. Tournassat, 2007. Modeling the composition of the pore
523 water in a clay-rock geological formation (Callovo-Oxfordian, France). Geochimica et
524 Cosmochimica Acta, **71**(5), 1087-1097. https://doi.org/10.1016/j.gca.2006.11.009.
525 Madsen, F. T, 1998, Clay Mineralogical Investigations Related to Nuclear Waste Disposal.
526 *Clay Minerals* 33 (1): 109–29. https://doi.org/10.1180/000985598545318.
527 Martin, T. 2012, Complex resistivity measurements on oak, European Journal of wood and
528 wood products, **70**, 45-53, https://doi.org/10.1007/s00107-010-0493-z.
529 Martin, T., Nordsiek, S., Weller, A., 2015, Low-frequency impedance spectroscopy of wood,
530 Journal of Research in Spectroscopy, 910447.

Madsen, F. T., 1998, Clay Mineralogical investigations related to nuclear waste disposal: Clay Minerals, **33** (1), 109–29. https://doi.org/10.1180/000985598545318.

Misra S., C. Torres-Verdín, A. Revil, J. Rasmus, and D. Homan, 2016, Interfacial polarization of disseminated conductive minerals in absence of redox-active species. Part 1: Mechanistic model and validation, Geophysics, **81**(2), E139-E157. https://doi.org/10.1190/GEO2015-0346.1.

Mokni, N., Barnichon J.-D., Dick P., Son Nguyen T., 2016, Effect of technological macro voids on the performance of compacted bentonite/sand seals for deep geological repositories. International Journal of Rock Mechanics and Mining Sciences, **88**, 87-97, ISSN 1365-1609. https://doi.org/10.1016/j.ijrmms.2016.07.011.

Molinero Guerra, A., N. Mokni, P. Delage, Y-J. Cui, A.M. Tang, P. Aimedieu, F. Bernier, and M. Bornert, 2017, In-Depth characterisation of a mixture composed of powder/pellets MX-80 Bentonite: Applied Clay Science, **135**, 538–46. https://doi.org/10.1016/j.clay.2016.10.030.

Müller-Vonmoos, M., Kahr, G., 1983, Mineralogische Untersuchungen von Wyoming Bentonit MX-80 und Montigel. Report. *Technischer Bericht NTB*. Vol. 83–12. ETH Zurich. https://www.research-collection.ethz.ch/handle/20.500.11850/114578.

Norris, S., 2017. Radioactive waste confinement: clays in natural and engineered barriers – introduction. Geological Society, London, Special Publications, **443**, 1–8. https://doi.org/10.1144/SP443.26.

Ntarlagiannis D., Wu Y., Ustra A.T., 2019, Special issue: recent developments in induced polarization, Near Surface Geophysics, **17**(6), 579.

Okay G., Cosenza P., Ghorbani A., Camerlynck C., Cabrera J., Florsch N., Revil A., 2013, Characterization of macroscopic heterogeneities in clay-rocks using induced polarization: Field tests at the experimental underground research laboratory of Tournemire (Aveyron,

556 France). Geophysical Prospecting, **61**, 134-152, https://doi.org/10.1111/j.1365-
557 2478.2012.01054.x.
558 Okay, G., Leroy, P., Ghorbani, A., Cosenza, P., Camerlynck, C., Cabrera, J., Florsch, N., Revil,
559 A., 2014. Spectral induced polarization of clay-sand mixtures: Experiments and modelling.
560 Geophysics, **79**, E353–E375. https://doi.org/10.1190/geo2013-0347-1.
561 Okko, O., Rautjaervi, J., 2006, Evaluation of monitoring methods available for safeguards use
562 at Olkiluoto geological repository Report on Task FIN C 1572 of the Finnish Support
563 Programme to IAEA Safeguards (ISBN 952-478-163–8). Finland.
564 Olhoeft, G.R., 1981, Electrical Properties of Rocks. Physical properties of rocks and minerals.
565 17 pp.
566 Pettersson, S., and Loennerberg, B., 2008, Final repository for spent nuclear fuel in granite -
567 the KBS-3V concept in Sweden and Finland. Presented at the Proceedings of the
568 international technical conference on the practical aspects of deep geological disposal of
569 radioactive waste, Ceske vysoke uceni technicke, Fakulta stavebni, Czech Republic, p.
570 346.
571 Revil, A., Atekwana E., Zhang C., Jardani A., and Smith S., 2012. A new model for the spectral
572 induced polarization signature of bacterial growth in porous media. Water Resour. Res.,
573 **48**, W09545. https://doi.org/10.1029/2012WR011965.
574 Revil, A., 2012, Spectral induced polarization of shaly sands: Influence of the electrical double
575 layer. Water Resour. Res. **48**. https://doi.org/10.1029/2011WR011260.
576 Revil, A., 2013a, On charge accumulations in heterogeneous porous materials under the
577 influence of an electrical field. Geophysics, **78**, 4, D271–D291.
578 https://doi.org/10.1190/GEO2012-0503.1.
579 Revil, A., 2013b, Effective conductivity and permittivity of unsaturated porous materials in the
580 frequency range 1 mHz–1GHz. Water Resour. Res., **49**.

https://doi.org/10.1029/2012WR012700.

Revil A., Woodruff W.F., Torres-Verdín C., Prasad M., 2013a, Complex conductivity tensor of hydrocarbon-bearing shales and mudrocks. Geophysics, **78**, no. 6, D403-D418. https://doi.org/10.1190/GEO2013-0100.1.

Revil A., Eppehimer J.D., Skold M., Karaoulis M., Godinez L., Prasad M., 2013b, Low-frequency complex conductivity of sandy and clayey materials. Journal of Colloid and Interface Science, **398**, 193–209.

Revil, A., A. Binley, L. Mejus, and P. Kessouri, 2015, Predicting permeability from the characteristic relaxation time and intrinsic formation factor of complex conductivity spectra, Water Resour. Res., **51**, 6672–6700. https://doi.org/10.1002/2015WR017074.

Revil, A., Coperey A., Shao Z., Florsch N., Fabricius I. L., Deng Y., Delsman J.R, Pauw P.S., Karaoulis M., de Louw P. G. B., van Baaren E. S., Dabekaussen W., Menkovic A., Gunnink J. L., 2017c, Complex conductivity of soils: Water Resour. Res., **53**, 8, 7121-7147. https://doi.org/10.1002/2017WR020655.

Revil A., A. Soueid Ahmed, A. Coperey, L. Ravanel, R. Sharma, and N. Panwar, 2020. Induced polarization as a tool to characterize shallow landslides, Journal of Hydrology, **589**, 125369. https://doi.org/10.1016/j.jhydrol.2020.125369.

Revil A., Schmutz M., Abdulsamad F., Balde A., Beck C., Ghorbani A. Hubbard S. S., 2021, Field-scale estimation of soil properties from spectral induced polarization tomography, Geoderma, **403**, 115380. https://doi.org/10.1016/j.geoderma.2021.115380.

Sauzeat, E., Guillaume, D., Neaman, A., Dubessy, J., François, M., Pfeiffert, C., Pelletier, M., Ruch, R., Barres, O., Yvon, J. Villéras, F., 2001 ; Caractérisation minéralogique, cristallochimique et texturale de l'argile MX-80. Rapport ANDRA No. CRP0ENG, pp.01-001.

605 Schanz, T., Al-Badran, Y., 2014, Swelling pressure characteristics of compacted Chinese
606 Gaomiaozi bentonite GMZ01. Soils Found., 54 (4), 748-759.
607 Schön, J., 1996, Physical Properties of Rocks: Fundamentals and Principles of Petrophysics:
608 Elsevier. https://doi.org/10.1016/c2014-0-03002-x.
609 Seigel, H., Nabighian, M., Parasnis, D.S. & Vozoff, K., 2007, The early history of the induced
610 polarization method: The Leading Edge, **26**, 3, 312-321.
611 Siddiqua, S., Blatz, J., Siemens, G., 2018, Evaluation of the impact of pore fluid chemistry on
612 the hydromechanical behaviour of clay-based sealing materials. Can. Geotech. J., **48**, 2,
613 199-213.
614 Studds, P.G., Stewart, D.I., Cousens, T.W., 1998, The effects of salt solutions on the properties
615 of bentonite–sand mixtures. Clay Miner., **33**, 651-660.
616 Sun, D., Zhang, L., Zhang B., Li J., 2015, Evaluation and prediction of the swelling pressures
617 of GMZ bentonites saturated with saline solution. Appl. Clay Sci., **105**, 207-216.
618 Suzuki, S., Prayongphan, S., Ichikawa, Y., Chae, B., 2005. In situ observations of the swelling
619 of bentonite aggregates in NaCl solution. Appl. Clay Sci., **29**, 89-98
620 Tang, A.-M., Y.-J. Cui, Le, T.-T., 2008, A Study on the thermal conductivity of compacted
621 bentonites. Applied Clay Science, **41**, 3, 181–189.
622 https://doi.org/10.1016/j.clay.2007.11.001.
623 Tartrat Y. T., Revil A., Abdulsamad F., Ghorbani A., Jougnot D., Coperey A., Yven B., de la
624 Vaissière R., 2019, Induced polarization response of porous media with metallic particles
625 – Part 10. Influence of desiccation. Geophysics. **84**, 5, A43-W32.
626 https://doi.org/10.1190/geo2019-0048.1.
627 Vaudelet P., A. Revil, M. Schmutz, M. Franceschi, P. Bégassat, 2012, Induced polarization
628 signature of the presence of copper in saturated sands. Water Resources Research, **47**,
629 W02526. https://doi.org/10.1029/2010WR009310.

630 Villar, M., 2005. MX-80 Bentonite. Thermo-Hydro-Mechanical Characterisation Performed at
631 CIEMAT in the Context of the Prototype Project, Informes Técnicos Ciemat.
632 Villar, M.V., Lloret, A., 2008. Influence of dry density and water content on the swelling of a compacted
633 bentonite. Appl. Clay Sci., **39**, 38–49.
634 Vinegar, H.J. and Waxman M.H., 1984, Induced polarization of shaly sands. Geophysics, **49**,
635 1267-1287.
636 Volckaert, G., Sillen, X., Van Geet, M., Bernier, F., Mayor, J.C., Goebel, I., Bluemling, P.,
637 Frieg, B., and Su, K., 2004, Similarities and differences in the behaviour of plastic and
638 indurated clays. In Ruiz, P. Fernandez (Ed.). Radioactive Waste Management - Community
639 Policy and Research Initiatives The sixth international conference on the management and
640 disposal of radioactive waste - Euradwaste '04, (p. 955). France.
641 Waxman, M.H. and Smits, L.J.M., 1968, Electrical Conductivities in Oil-Bearing Shaly Sands:
642 Society of Petroleum Engineers Journal, **8**, 107-122. http://dx.doi.org/10.2118/1863-A.
643 Zhu, C.M., Ye, W.M., Chen, Y.G., Chen, B., Cui. Y.J., 2013, Influence of salt solutions on the
644 swelling pressure and hydraulic conductivity of compacted GMZ01 bentonite.
645 Engineering Geology, **166**, 74-80.
646

Tables

Table 1. Pore water conductivities (NaCl, 25°C) used in the calculation of the formation factor, cementation exponent and surface conductivity. The formation factor F and surface conductivity σ_s are determined from $\sigma_\infty = \sigma_w / F + \sigma_S$ the then Archie's law $F = \phi^{-m}$ is used to compute the power-law exponent m. The data given here correspond to saturated core samples.

ID	σ_w (S m^{-1})	σ' (S m^{-1})	ϕ (–)
E45	0.2	0.2835	0.553
E46	1.0	0.3161	0.544
E47	5.0	0.6111	0.526
E48	15	1.348	0.508
E28	0.0594 (*)	0.43789	0.519

(*) Using de-ionized water

Table 2. Mineralogy of Wyoming MX80 bentonite taken from various sources in the literature. Mo., montmorillonite; Q, quartz; F, feldspar; M, muscovite; T, tridymite; C, calcite. We see that montmorillonite is by far the most abundant component. The composition is given in Vol.%.

Source	Mo.	Q	F	M	T	C
Karnland et al. (2006)	81.4	3	3.5	3.4	3.8	0.2
Madsen (1998)	75.5	15	5-8	< 1	-	-
Molinero Guerra (2018)	80	4	10	4	-	-
Kumpulainen and Kiviranta (2010)	81.7	3.8	1.5	5.3	2.6	0.5
Kiviranta and Kumpulainen (2011)	88.2	3.5	5.5	0.3	-	0.2
Mueller-Vonmoos and Kahr (1983)	75	15.2	5-8	< 1	-	0.7
Sauzeat et al. (2001)	> 80	5-6	4.5	2.8-3.8	-	0.3-1.4
Tang et al. (2008)	92	3	-	-	-	-
Villar (2004)	65-82	4-12	5-8	-	-	-
Montes Hernandes et al. (2007)	70.6	2.5	1.8	-	-	0.7

662 **Table 3.** Results of the experiments. ID described the experiment number. Θ denotes the water
663 content. The quantities ρ_b and ρ_d denote the bulk density and the dry density, respectively. The
664 quantity ϕ denotes the connected porosity. Finally the quantities s' and s" denote the in-phase
665 conductivity determined at the frequency of 345 Hz and M_n denotes the normalized
666 chargeability taken as the difference in the in-phase conductivity between 10 Hz and 10 kHz.
667 Experiments E45 to E48 (between 90 – 100 % saturation) are performed using pore water
668 conductivities of 0.2, 1.0, 5.0, and 15 S m^{-1} (NaCl, 25°C).

ID	Θ (-)	Sw (-)	ρ_b (g cm^{-3})	ρ_d (g cm^{-3})	ϕ (-)	σ' (S m^{-1})	σ'' (S m^{-1})	M_n (S m^{-1})
E1	0.174	0.465	1.91	1.73	0.374	0.03572	0.00042	0.00209
E3	0.155	0.344	1.68	1.52	0.450	0.00778	0.00008	0.00031
E4	0.159	0.371	1.74	1.58	0.429	0.01603	0.00019	0.00085
E5	0.185	0.545	2.02	1.83	0.339	0.04408	0.00055	0.00272
E6	0.209	0.417	1.59	1.38	0.501	0.03060	0.00009	0.00025
E7	0.222	0.464	1.67	1.45	0.478	0.05112	0.00019	0.00076
E8	0.25	0.617	1.9	1.65	0.405	0.06770	0.00023	0.00124
E9	0.234	0.525	1.77	1.54	0.445	0.10428	0.00049	0.00239
E10	0.274	0.541	1.64	1.37	0.506	0.04843	0.00009	
E11	0.298	0.619	1.73	1.44	0.482	0.09293	0.00019	
E12	0.311	0.703	1.85	1.54	0.443	0.18208	0.00043	0.00377
E13	0.344	0.897	2.05	1.71	0.384	0.26431	0.00056	0.00419
E14	0.368	0.661	1.59	1.23	0.557	0.15942	0.00034	
E15	0.396	0.751	1.71	1.31	0.527	0.19961	0.00044	0.00067
E16	0.417	0.821	1.78	1.36	0.507	0.24866	0.00065	0.00276
E17	0.42	0.842	1.81	1.39	0.499	0.26774	0.00051	0.00120
E18	0.424	0.858	1.82	1.40	0.494	0.26535	0.00063	0.00174
E19	0.427	0.868	1.83	1.41	0.492	0.24592	0.00049	
E20	0.429	0.878	1.85	1.42	0.488	0.27945	0.00064	0.00131
E21	0.435	0.899	1.86	1.43	0.484	0.28673	0.00082	0.00139
E22	0.338	0.536	1.36	1.03	0.630	0.07712	0.00019	
E23	0.408	0.645	1.43	1.02	0.632	0.20415	0.00111	0.00284
E24	0.457	0.779	1.6	1.14	0.587	0.22167	0.00086	0.00366
E25	0.5	0.900	1.73	1.23	0.556	0.33016	0.00156	0.00085
E26	0.513	0.956	1.8	1.28	0.537	0.29059	0.00110	0.00644
E27	0.516	0.96	1.8	1.28	0.538	0.36324	0.00124	0.00322
E28	0.536	1.033	1.87	1.33	0.519	0.43789	0.00204	0.00776
E29	0.539	1.045	1.88	1.34	0.516	0.39644	0.00203	0.00535
E30	0.544	1.067	1.9	1.36	0.510	0.42740	0.00175	0.00505
E31	0.456	0.677	1.36	0.91	0.673	0.13063	0.00080	0.00100
E32	0.564	0.945	1.68	1.12	0.597	0.33575	0.00209	0.00624
E33	0.417	0.554	1.1	0.68	0.753	0.13658	0.00115	0.00523
E34	0.484	0.68	1.28	0.8	0.712	0.18436	0.00153	0.00584
E35	0.546	0.809	1.44	0.9	0.675	0.23146	0.00180	0.00749
E36	0.592	0.914	1.57	0.97	0.648	0.30978	0.00264	0.01194
E37	0.597	0.931	1.59	0.99	0.642	0.33401	0.00231	0.00988
E38	0.661	1.096	1.76	1.1	0.603	0.32784	0.00230	0.00848
E39	0.536	0.738	1.29	0.76	0.727	0.17697	0.00171	0.00857
E40	0.686	1.057	1.66	0.97	0.649	0.44600	0.00361	0.01497
E41	0.485	0.621	1.09	0.61	0.782	0.18240	0.00197	0.00995
E42	0.606	0.834	1.36	0.76	0.727	0.31642	0.00374	0.01915
E43	0.708	1.036	1.58	0.88	0.683	0.41971	0.00363	0.01432
E44	0.701	0.936	1.39	0.7	0.749	0.32564	0.00399	0.01962
E45	0.498	0.90	1.73	1.09	0.553	0.283579	0.001621	0.007877
E46	0.506	0.93	1.77	1.09	0.545	0.316158	0.001881	0.008886

E47	0.527	1.003	1.84	1.31	0.526	0.61116	0.002642	0.010086
E48	0.552	1.087	1.91	1.36	0.508	1.348184	0.002354	0.008883
E49	0.528	1.003	1.84	1.31	0.526	0.29833	0.00140	0.00308
E50	0.516	0.962	1.8	1.28	0.537	0.34092	0.00172	0.00573
E51	0.303	0.667	1.81	1.51	0.455	0.11818	0.00020	
E52	0.645	1.05	1.71	1.07	0.614	0.42300	0.00341	0.01381
E53	0.636	0.959	1.57	0.93	0.663	0.25208	0.00168	0.00373
E54	0.673	1.046	1.66	0.99	0.644	0.36752	0.00243	0.00864
E55	0.381	0.697	1.64	1.26	0.547	0.15759	0.00046	
E56	0.324	0.528	1.39	1.07	0.615	0.06587	0.00015	
E57	0.460	1.015	1.97	1.52	0.453	0.30526	0.00095	
E58	0.454	0.989	1.95	1.50	0.460	0.27284	0.00073	
E59	0.420	0.840	1.80	1.39	0.500	0.16190	0.00037	
E60	0.715	1.023	1.55	0.83	0.699	0.39047	0.00244	
E61	0.729	1.052	1.58	0.85	0.693	0.33581	0.00248	0.00961
E62	0.705	1.002	1.52	0.82	0.703	0.36939	0.00302	
E63	0.463	0.736	1.49	1.03	0.630	0.13881	0.00056	
E64	0.538	0.945	1.73	1.19	0.570	0.22339	0.00086	
E65	0.515	0.875	1.65	1.14	0.588	0.22110	0.00099	
E66	0.559	1.011	1.80	1.24	0.553	0.33062	0.00161	
E67	0.239	0.566	1.84	1.60	0.423	0.02765	0.00013	
E68	0.691	1.090	1.70	1.01	0.634	0.38463	0.00241	0.00824
E69	0.691	1.094	1.71	1.02	0.632	0.32466	0.00203	0.00562

669
670

671

Figures

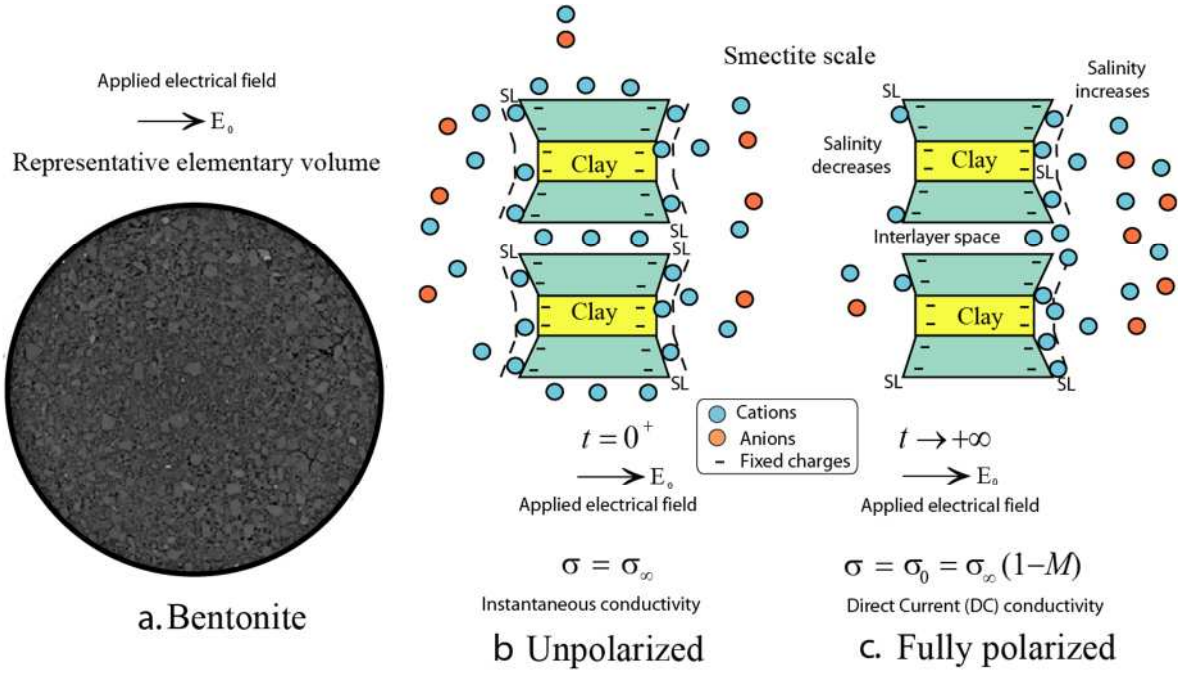

Figure 1. Polarization of bentonite associated with the application of the field $\mathbf{E}_0$. **a.** Bentonite core sample with clays and coarser grains. **b.** At the size of the crystal, a clay particle is coated by an electrical double layer with a diffuse later and a compact layer called the Stern layer (SL stands for the Stern Layer). Just upon the application of the field $\mathbf{E}_0$ (i.e., (at t=0+) all the charge carriers are mobile. Therefore, they all contribute to the surface conductivity. The instantaneous conductivity σ_∞ corresponds to this state. **c.** When the external electrical field has been applied for a long time, the clay particles are polarized. The ionic charge carriers associated with clay polarization do not contribute to the conduction process. The conductivity is the Direct Current (DC) conductivity $\sigma_0 < \sigma_\infty$. M (dimensionless) denotes the chargeability.

687

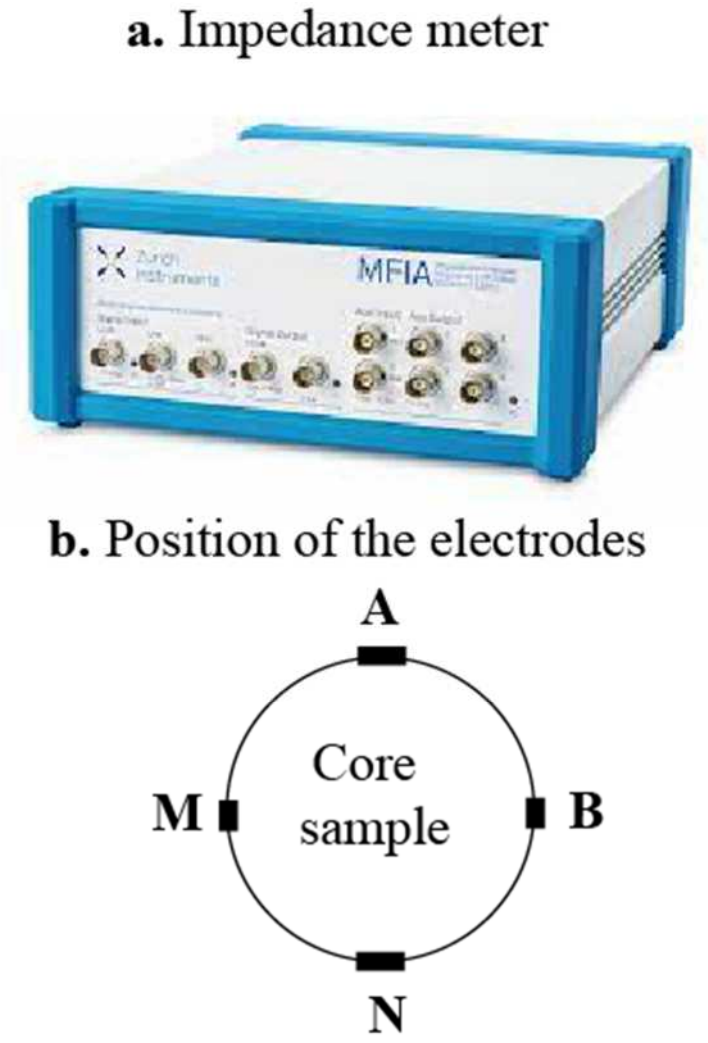

688
689
690 **Figure 2.** Experimental setup. **a.** Impedance meter from Zurich Instrument used for the
691 complex conductivity measurements in the frequency range 1 Hz-45 kHz. **b.** Position of the
692 electrodes on the side of the core sample (A and B are current electrodes; M and N are potential
693 measurement electrodes).
694

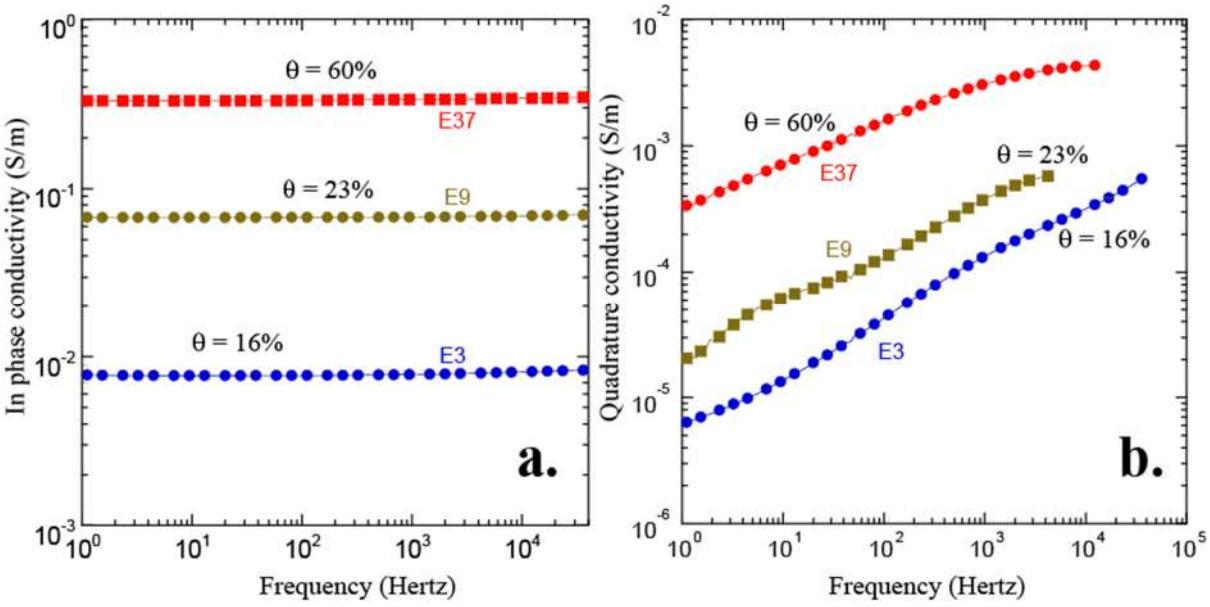

695
696

697 **Figure 3.** In-phase and quadrature conductivity spectra of three core samples characterized by
698 distinct water contents (here expressed in Vol.%). **a.** In phase conductivity spectra. **b.**
699 Quadrature conductivity spectra.
700

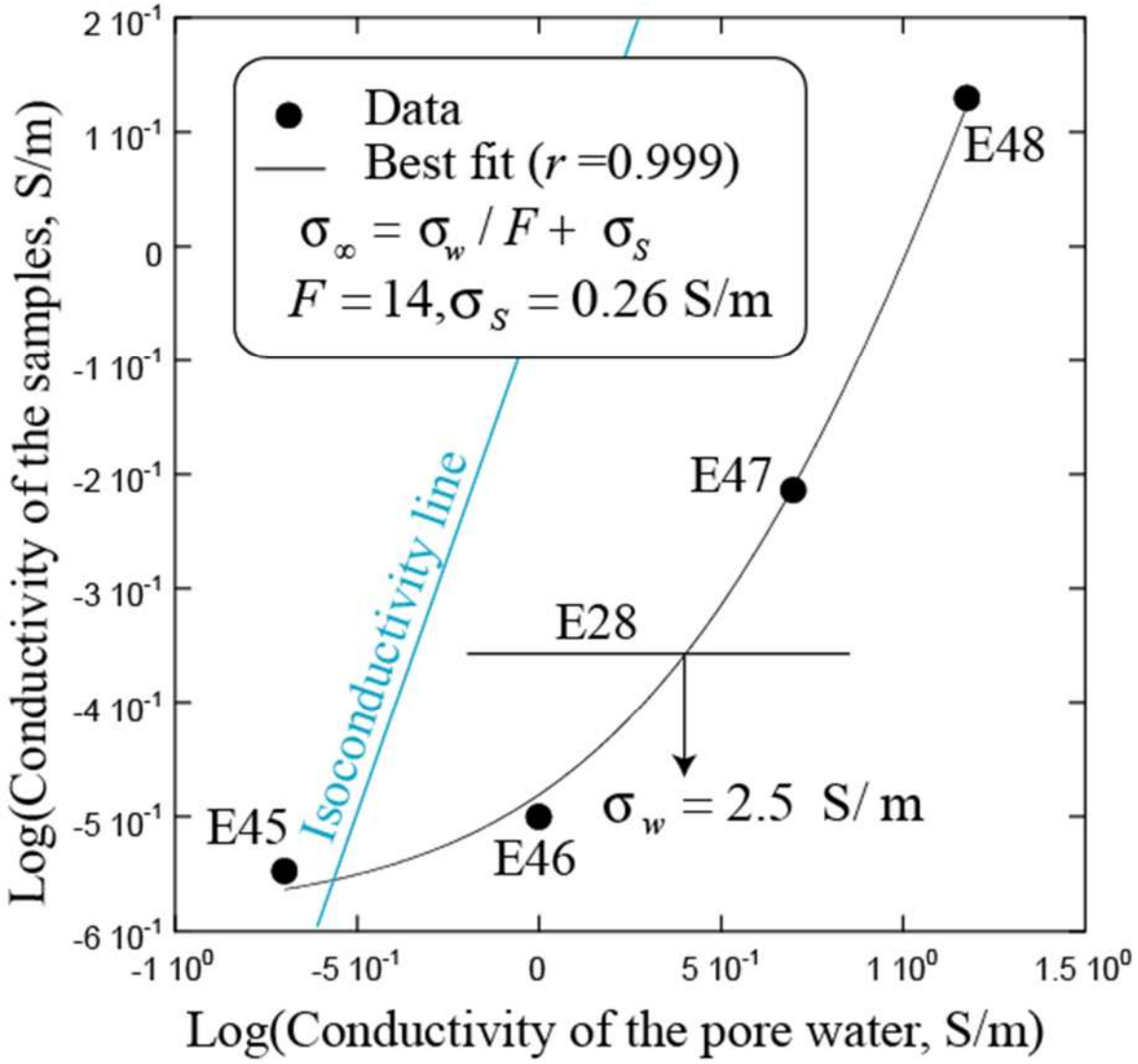

Figure 4. Conductivity of the saturated samples versus the conductivity of the pore water at saturation and for a porosity of 0.53±0.02 (data from Table 1). Sample E28 (also fully water-saturated) is also saturated with distilled water. It is at the same porosity than the other core sample (around 0.52). It indicates that the real conductivity of the pore water is around 2.5 S m^{-1} (25°C). The value of the formation factor and the porosity (0.53±0.02) yields a porosity exponent m = 4.5. The isoconductivity line is the line for which the conductivity of the core sample is equal to the conductivity of the pore water. This corresponds to the limit of the linear (high salinity) conductivity model used in the main text.

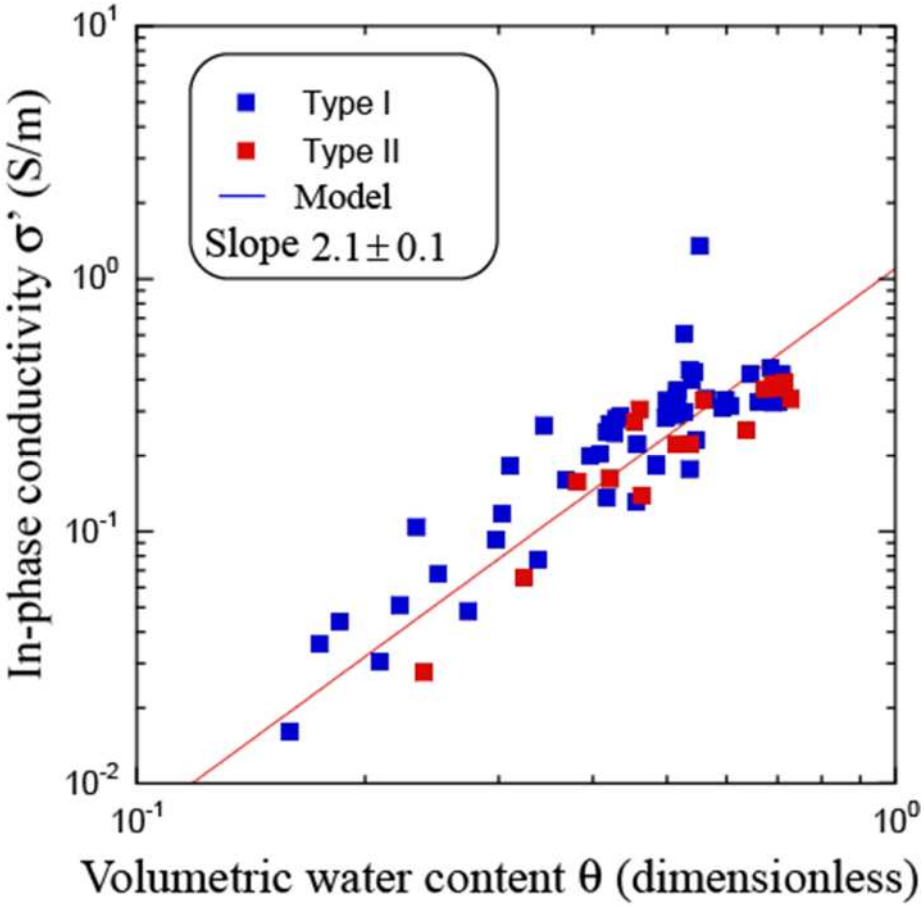

Figure 5. Dependence of the in-phase conductivity versus the water content (r = 0.82). The data are fitted with a power law function. The prefactor determined from the linear regression is equal to 1.1±0.1 S m^{-1} close to the predicted value of $a' = \Sigma_S$ = 0.8 S m^{-1} The slope determined from the best fit is equal to a power-law exponent of 2.1 ± 0.1, much lower however than the cementation exponent determined from the porosity and formation factor (m = 4.2).

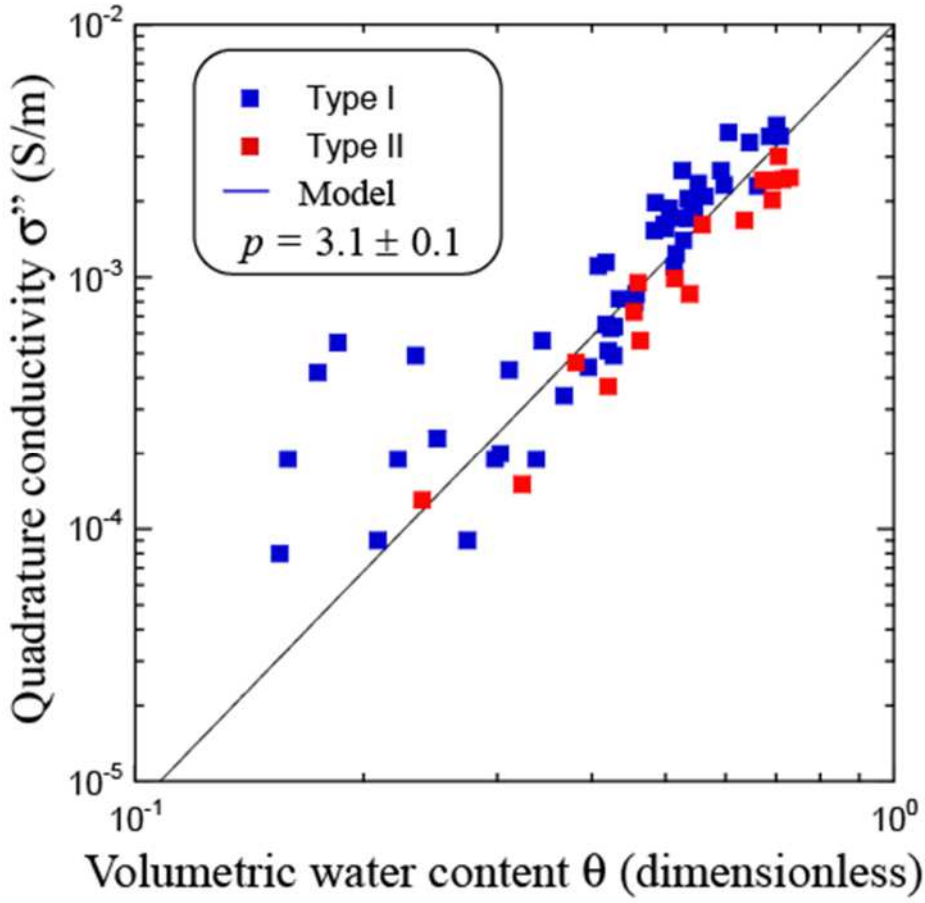

Figure 6. Dependence of the quadrature conductivity versus the water content (r = 0.74). The data are fitted with a power-law function. The prefactor is equal to 0.0100±0.0004 S m^{-1} close to the theoretical prefactor determined in the main text and given by $a'' = \Sigma_S R/\alpha$ = 0.0095 S m^{-1}. The porosity exponent is equal to $p = 3.1 \pm 0.1$ fairly consistent with the expression $p = m - 1$ and m = 4.5 determined from the formation factor and the porosity (see Figure 4).

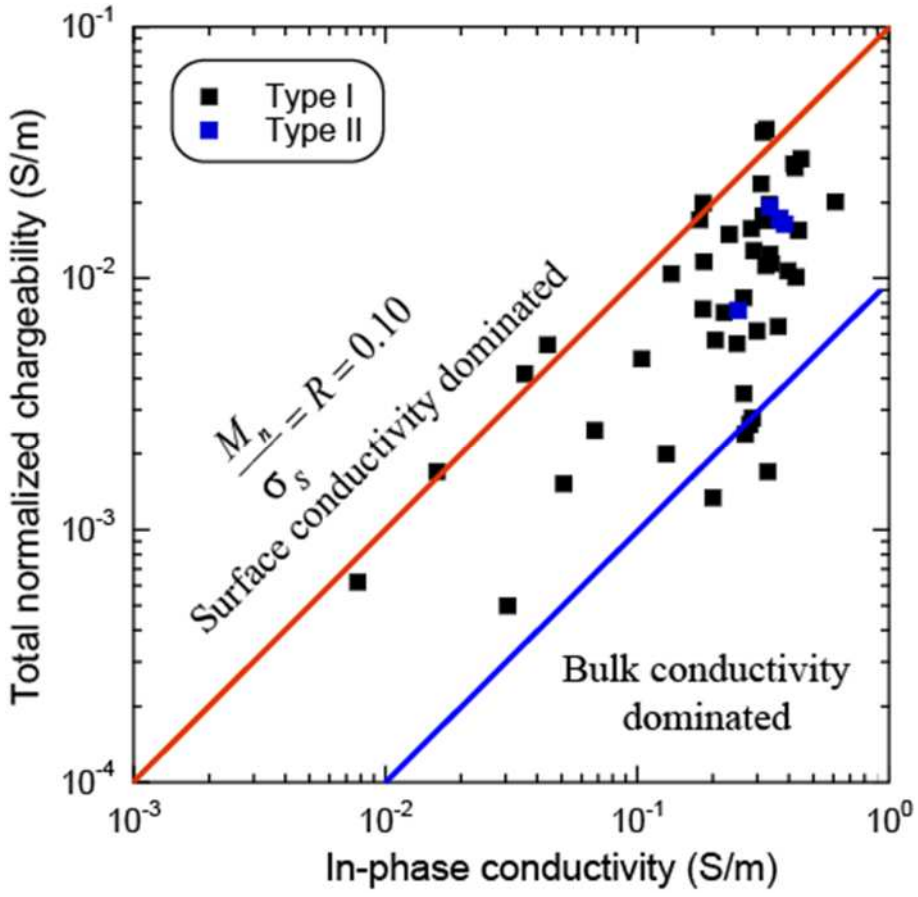

Figure 7. Normalized chargeability (twice the normalized chargeability determined from the difference in the conductivity between 1 Hz and 10 kHz) versus the in-phase conductivity. The plot shows that for some experiments, surface conductivity dominates the bulk conductivity and the data points are close to the red straight line. That said, there are experiments for which this is not the case and the data are close or below the blue line for which the bulk conductivity is ten times higher than the surface conductivity. These results are consistent with a high value of the pore water conductivity (2.5 S m^{-1} at 25°C).

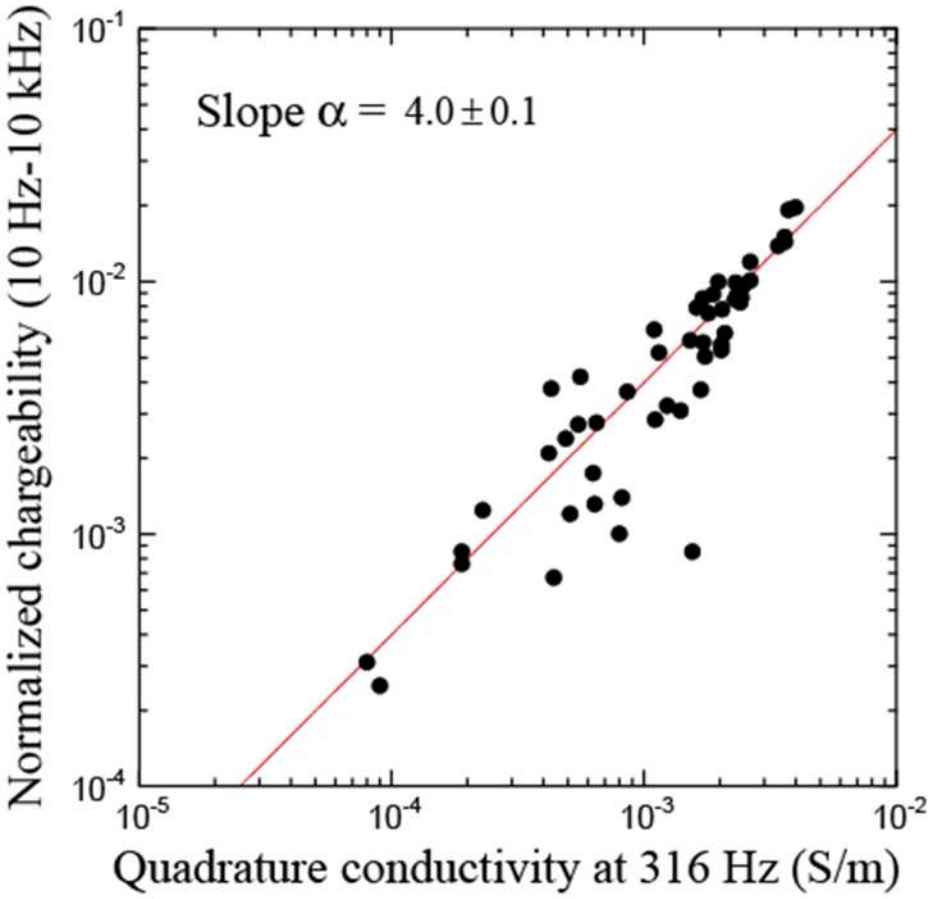

Figure 8. The normalized chargeability (taken here as the difference of the in-phase conductivity between 10 hertz and 10 kHertz) versus the quadrature conductivity (at the geometric mean of the two frequency, 316 Hertz) for the core samples of Table 3 (r = 0.69). The predicted slope is given by $\alpha = -(2/\pi)\ln D \approx 4.4$ close to the one obtained through a linear regression ($\alpha = 4.0$). Consequently, the normalized chargeability obeys to the same dependence with the water content than the quadrature conductivity.

765

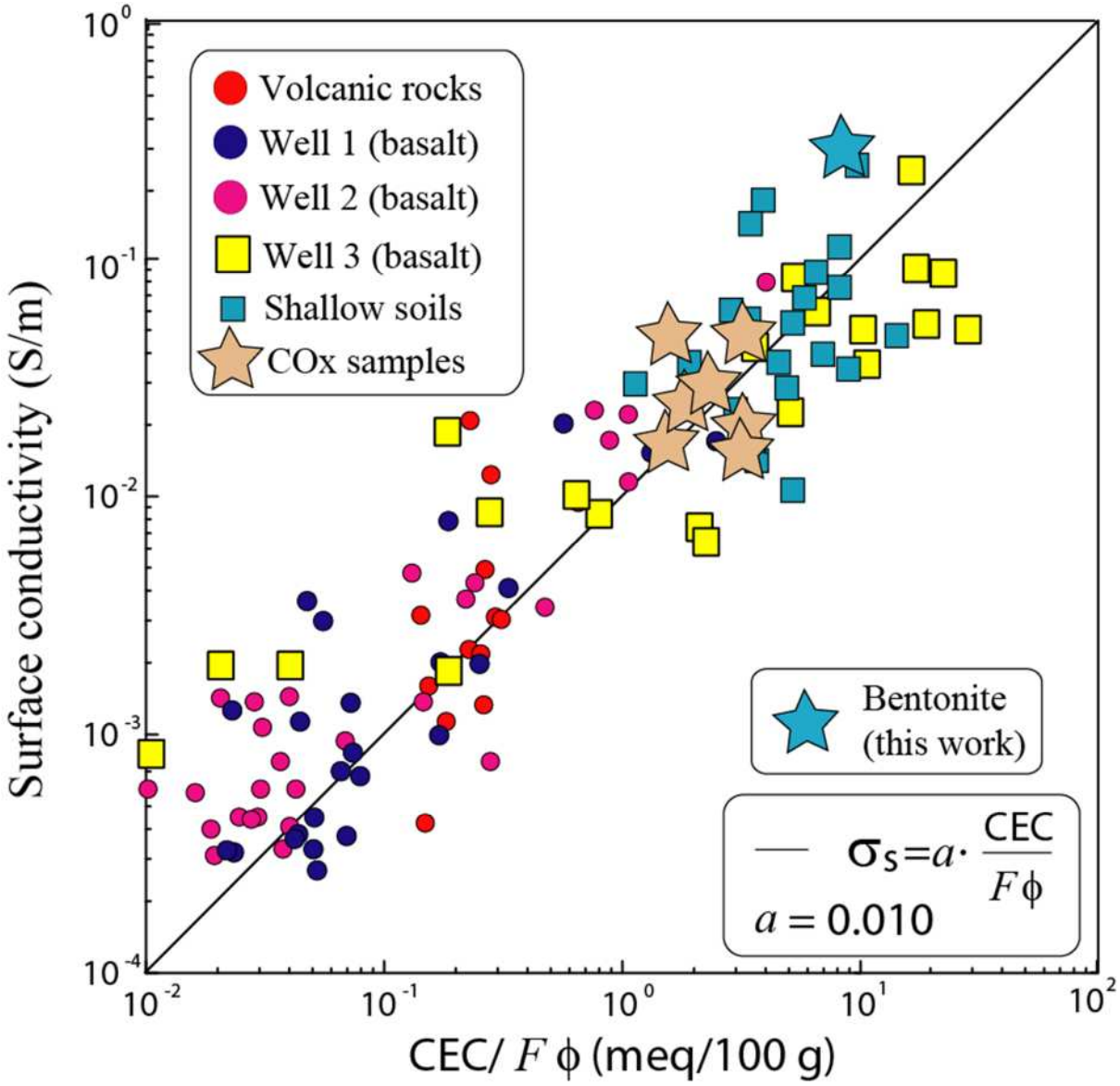

766
767
768

769 **Figure 9.** Surface conductivity versus the reduced CEC (CEC divided by the bulk tortuosity
770 defined by the product of the formation factor and the connected porosity). COx stands for
771 Callovo-Oxfordian clayrocks from the Paris Basin. The data on the volcanic rocks are from
772 Revil et al. (2018), Ghorbani et al. (2018), and Revil et al. (2021b). The MX80 bentonite is
773 characterized by the highest surface conductivity of the dataset (r = 0.72 for the dataset).
774

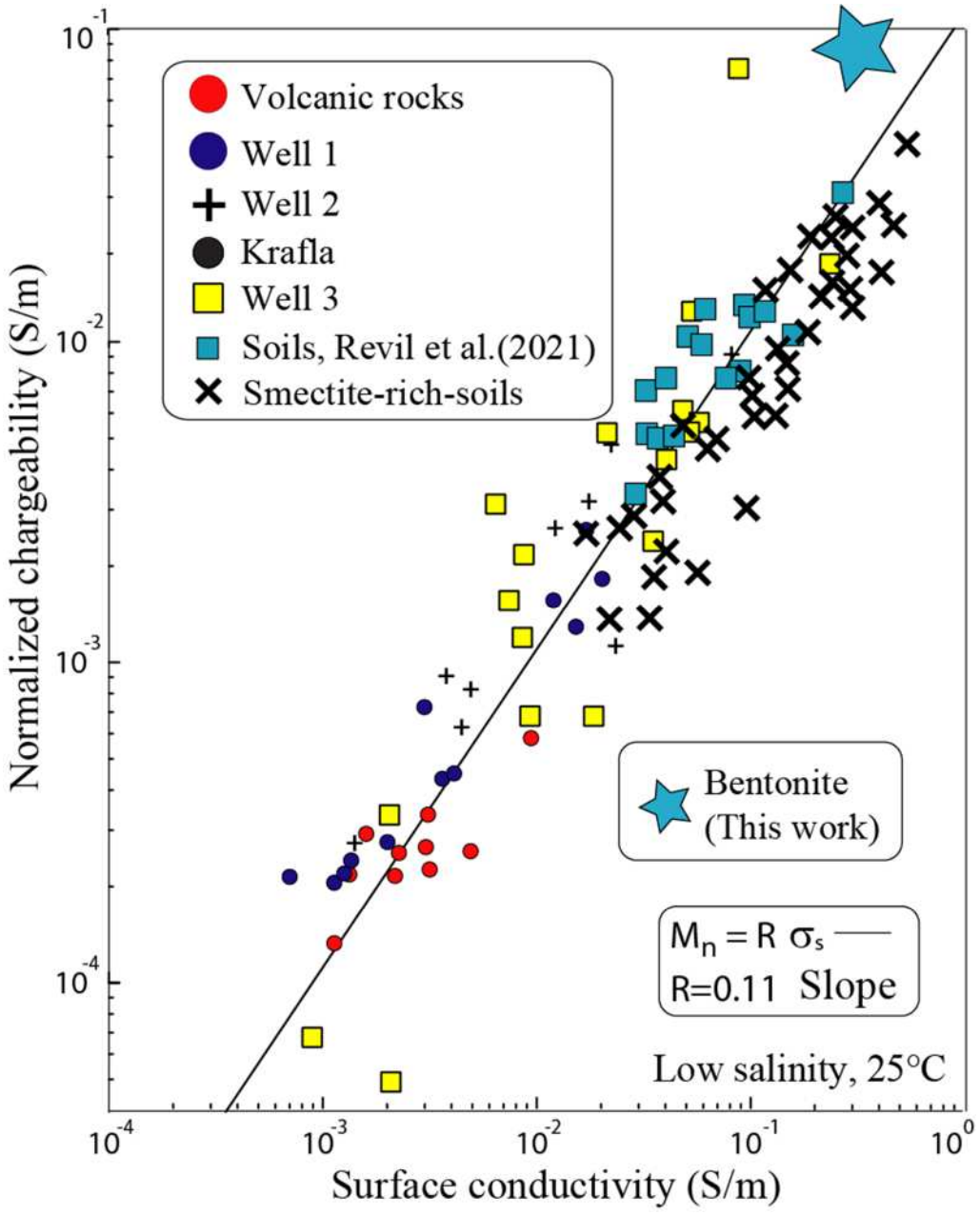

Figure 10. Relationship between normalized chargeability and surface conductivity. Comparison between the soil samples of the present study, the smectite-rich soil samples from the study of Revil et al. (2017) and volcanic rock samples (consolidated and not consolidated) from Hawaii and Krafla volcanoes (in Iceland, see Revil et al., 2018 and Ghorbani et al., 2018) excluding core samples with magnetite or pyrite. The slope of the trend provides the value of the fundamental dimensionless coefficient R, which is consistent with previous estimates of this parameter. Data from Revil et al. (2021b, volcanic rocks) and Revil et al. (2017, smectite-rich soils). For the MX80 bentonite, the surface conductivity is equal to ~0.26 S m^{-1} and the normalized chargeability is ~0.01 S m^{-1}. The MX80 bentonite is characterized by the highest normalized chargeability of the entire dataset (r = 0.83 for the dataset).

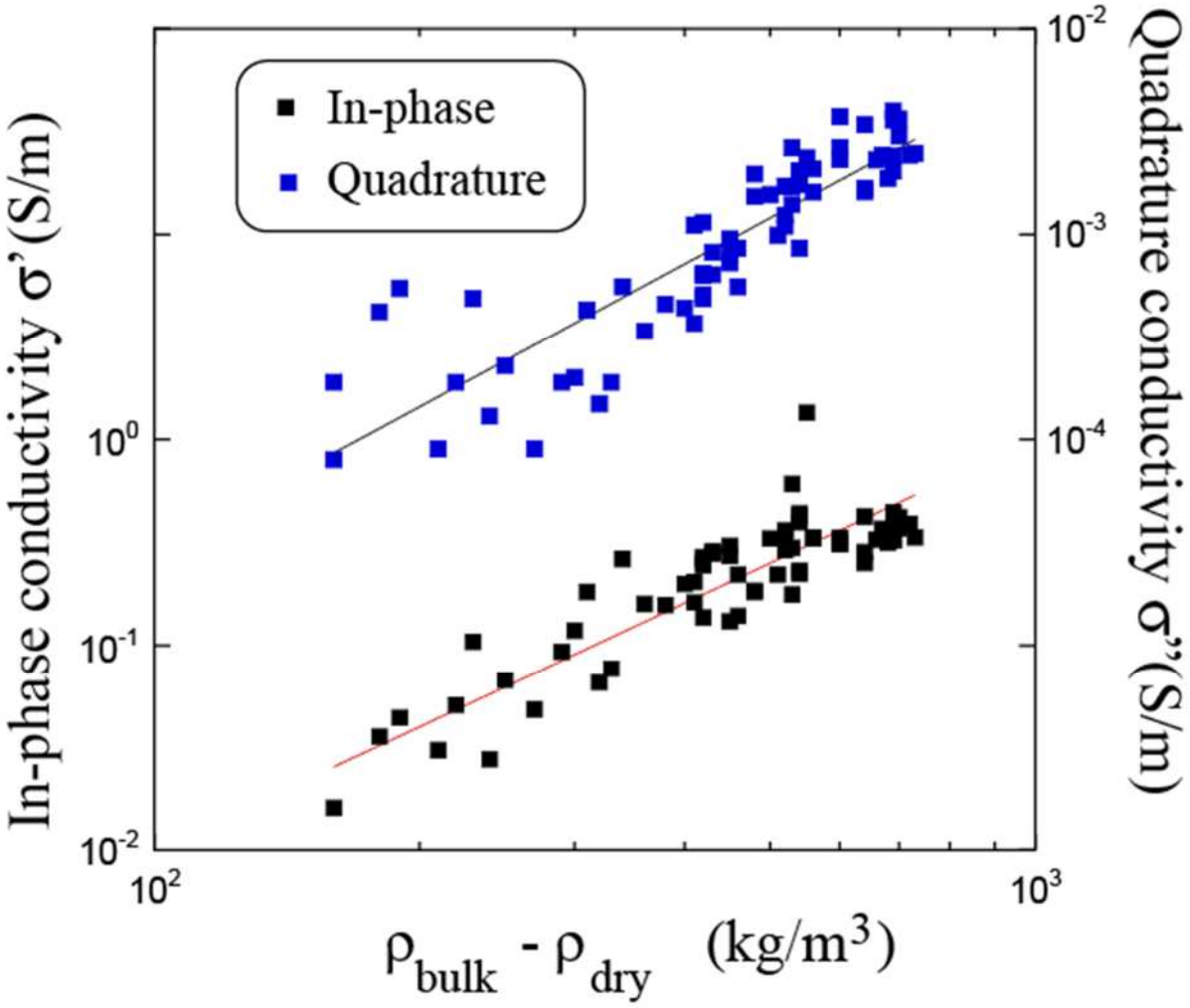

Figure 11. Relationship between the in-phase and quadrature conductivity versus the difference between the bulk and dry densities (correlation coefficient *r* of 0.60 and 0.86 respectively). .